THE ASTROPHYSICAL JOURNAL, 564:244–259, 2002 January 1

MEASUREMENT OF COSMIC-RAY HYDROGEN AND HELIUM AND THEIR ISOTOPIC COMPOSITION WITH THE BESS EXPERIMENT

J. Z. WANG AND E. S. SEO
Institute for Physical Science and Technology, University of Maryland, College Park, MD 20742
K. ANRAKU, M. FUJIKAWA, M. IMORI, T. MAENO, N. MATSUI, H. MATSUNAGA, M. MOTOKI, S. ORITO,[1] T. SAEKI, T. SANUKI, I. UEDA, AND K. YOSHIMURA
University of Tokyo, Tokyo 113-0033, Japan
Y. MAKIDA, J. SUZUKI, K. TANAKA, A. YAMAMOTO, AND T. YOSHIDA
KEK, Tsukuba, Ibaraki 305-0801, Japan
T. MITSUI, H. MATSUMOTO, M. NOZAKI, AND M. SASAKI
Kobe University, Kobe, Hyogo 657-8501, Japan
J. MITCHELL, A. MOISEEV, J. ORMES, AND R. STREITMATTER
NASA Goddard Space Flight Center, Code 660, Greenbelt, MD 20771
AND
J. NISHIMURA, Y. YAJIMA, AND T. YAMAGAMI
Institute for Space and Astronautical Science, Sagamihara, Kanagawa 229-8510, Japan
Received 2001 February 7; accepted 2001 August 31

ABSTRACT

The cosmic-ray hydrogen and helium spectra have been measured by the Balloon Borne Experiment with a Superconducting Solenoid Spectrometer (BESS), which has been flown from Lynn Lake, Manitoba, Canada, annually since 1993. The BESS experiment provides excellent rigidity measurement and precise particle identification with a large geometric acceptance. We present here the hydrogen and helium nuclei energy spectra from 0.2 to 10 GeV nucleon^{-1} and their isotopic composition from 0.2 to about 1 GeV nucleon^{-1} for the first BESS flight. This provides the first simultaneous measurements of the cosmic-ray secondaries, deuterons, and ^{3}He, with their primaries, protons, and ^{4}He over this energy range in a period of solar minimum. In this paper, we have achieved significant improvements in data analysis in the following aspects. First, the latest available cross-section data and their parameterizations were utilized in the simulation code developed for this study. Second, a complete simulation was performed for both protons and heavy ions: the δ-ray effect was properly simulated and showed a large influence on the measurement of heavy ions at high energies. Third, the secondary particle correction, which dominates the systematic uncertainty at low energies for singly charged particles, protons and deuterons, was calculated iteratively with the simultaneously measured primary cosmic-ray spectra. In general, the results of this experiment are consistent with other recent measurements using balloon-borne or satellite experiments, but with better precision. The measured spectra of protons, deuterons, ^{3}He, and ^{4}He and their corresponding ratios are compared with different interstellar/heliospheric propagation calculations, which were derived to fit observations of heavy nuclei. The overall good agreement indicates that the propagation history for light cosmic-ray elements, protons, deuterons, and helium nuclei is similar to that of the heavy nuclei. The ^{2}H/^{1}H ratio is sensitive to the propagation models, and our results show a tendency of better agreement with the reacceleration model than the standard leaky-box model.

Subject headings: balloons — cosmic rays — elementary particles — nuclear reactions, nucleosynthesis, abundances

1. INTRODUCTION

Cosmic-ray particles are a unique sample of deep-Galaxy matter that can be measured on Earth. Protons and helium nuclei are the most abundant components among the primary cosmic-ray particles. Their isotopes, ^{2}H and ^{3}He, are rare and are generally believed to be secondary particles from nuclear interactions of primary cosmic rays with the interstellar medium. Precise measurements of their absolute abundance, their isotopic composition, and the exact shape of their energy spectra are of particular astrophysical importance for several reasons:

1. Cosmic-ray fluxes in the interstellar medium, which in principle can be derived from local measurements by demodulating the observed spectra for solar modulation, are important for understanding the Galactic propagation and acceleration mechanisms of cosmic rays.

2. Deuteron and ^{3}He secondaries offer better statistics than other secondaries, antiprotons and positrons, and their simultaneous measurement with their major primaries is expected to provide important information about particle propagation history in the Galaxy.

3. Precise knowledge of proton and helium spectra and fluxes in the interstellar medium is critical for interpretation of antiproton and antihelium data, which is the primary goal of several current cosmic-ray experiments (BESS:

[1] Deceased.

Yoshimura et al. 1995, Moiseev et al. 1997, Matsunaga et al. 1998, Orito et al. 2000, Maeno et al. 2001; IMAX: Mitchell et al. 1996; CAPRICE: Boezio et al. 1997, etc.).

4. Knowledge about the proton and helium spectra at the top of the atmosphere (TOA) is required for calculations that aim to predict many atmospheric secondary particles, such as atmosphere neutrinos (Honda et al. 1995; Circella et al. 1997), γ-rays (Bertsch et al. 1993; Mori 1997), positrons (Golden 1996), deuterons (Webber et al. 1991; Papini, Grimani, & Stephens 1993b; Wefel et al. 1995b) and ^{3}He (Papini et al. 1993a), etc. Precise knowledge of the primary flux reduces the uncertainty in secondary flux calculations.

The Balloon Borne Experiment with a Superconducting Solenoid Spectrometer (BESS), which has been flown annually since 1993, has measured both cosmic-ray hydrogen and helium, as well as their isotopes. Monte Carlo simulations were used to fully understand the BESS instrument and to obtain the absolute fluxes. The available cross section data were compiled, and suitable hadronic packages for heavy ion simulations were selected for the study presented.

In particular, in this paper we present the absolute fluxes of hydrogen and helium from 0.2 to 10 GeV nucleon^{-1} and their isotopic composition from 0.2 to about 1 GeV nucleon^{-1} obtained from the first flight, BESS 93. The high-energy proton and helium energy spectra measured by BESS were presented in a separate paper (Sanuki et al. 2000). Likewise, BESS results on antiprotons (Yoshimura et al. 1995; Moiseev et al. 1997; Matsunaga et al. 1998; Orito et al. 2000; Maeno et al. 2001, etc.) and antihelium upper limit (Ormes et al. 1997; Saeki et al. 1998; Nozaki et al. 1999, etc.) have already been published. Preliminary results on hydrogen, helium, and their isotopes measurement from this experiment were reported earlier (Seo et al. 1995, 1997a, 1997b, 2000; Wang et al. 1999). Here we provide the analysis details, the adopted procedural improvements, and the final results.

2. BESS 93 EXPERIMENT

2.1. *BESS 93 Instrument*

BESS (Fig. 1) is a balloon-borne instrument, which measures the cosmic-ray rigidity using a superconducting solenoidal magnet. For a detailed instrument description, refer to the extensive instrument papers (Orito 1987; Yamamoto et al. 1994; Ajima et al. 2000; and references therein). A typical event measured by BESS passes through, from top to bottom, a pressure vessel (PV), a time-of-flight scintillator hodoscope (TOF), outer drift chambers (ODC), a superconducting solenoid (MAG), inner drift chambers (IDC), a central jet-type drift chamber (JET), and the symmetric bottom half of the instrument. Redundant detection techniques are used to measure three important parameters of individual cosmic rays: charge, mass, and energy. With many outstanding features, illustrated below, BESS can achieve cosmic-ray measurements with high precision.

2.1.1. *Large Geometry Acceptance*

The spectrometer has a compact cylindrical structure, which allowed it to possess a large geometry acceptance of 0.42 m^2 sr for BESS 93. This geometry factor is an order of magnitude larger than those of the similar balloon-borne magnet spectrometers used previously or currently being used in the cosmic-ray measurements (LEAP: Seo et al. 1991; HEAT: Barwick et al. 1998; CARPRICE: Boezio et al. 1999; IMAX: Menn et al. 2000, etc.). Over the entire measured energy range above 0.2 GeV nucleon^{-1}, the energy dependence of the geometry factor is less than 5%, which is also a unique feature of BESS compared to the other balloon magnet spectrometers. BESS is able to measure antimatter as well as positive-charge nuclei with very high statistical accuracy.

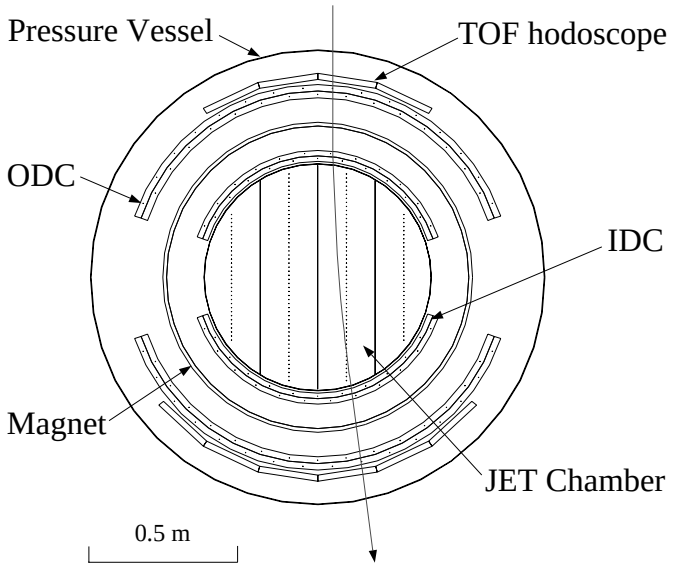

FIG. 1.—Basic configuration of the BESS 93 instrument with one simulated proton event.

2.1.2. *Uniform and High-Intensity Magnet*

The superconducting solenoid produces a strong magnetic field of 1 Tesla in the cylinder. The field nonuniformity is better than $\pm 15\%$ inside the entire cylinder and better than $\pm 7\%$ in the fiducial volume ($|z| < 430$ mm), which again is the best compared to all other balloon-borne magnet spectrometers. With this uniform magnet, the reconstruction of rigidity is much simpler and more reliable; therefore, BESS can provide very accurate rigidity measurements of charged particles.

2.1.3. *Fine Segmentation*

A JET chamber, 0.754 m in diameter and 1 m in length, is located inside the magnet coil. The chamber volume is divided into four sections by the cathode planes as shown in Figure 1. There are 52 sense wires in each of the two inner sections. Among them, 24 wires are read out for the position measurements in the r-ϕ plane and 16 wires are read out from both sides to provide position determination along the z-axis. Each of the two outer sections has 32 sense wires and provides 16 measurements in the r-ϕ plane and eight measurements along the z-axis. The digitized signals from the sense wires is discriminated by a digital comparator for the zero-suppression. Only the signals above the threshold are saved as "hits."

The IDC and ODC are arc-shaped drift chambers located inside and outside the magnet coil, respectively (Fig. 1). The two chambers are identical except for their dimension. Each of them is divided into two layers. At the center of each layer, sense wires and field wires are alternately laid out in about 50 mm spacing intervals. There is a total of 44 sense wires in the IDC and 62 in the ODC.

The tracking in the bending plane was performed by fitting up to 28 hit points (24 JET hits plus 4 IDC hits) each with a spatial resolution of 200 μm. The maximum detectable rigidity (MDR) of this system is 200 GV, and the momentum resolution is 0.5% at 1 GeV/c. With the fine segmentation, JET, IDC, ODC, and TOF are all equipped with multi-hit identification capability to clearly distinguish the multitrack events that have nuclear interactions inside the instrument.

2.1.4. *Good Resolution of TOF and dE/dx Measurement*

The TOF hodoscope contains two counters situated on the outer surface of the ODC. The upper one is divided into four paddles and the low one into six paddles. For the position determination along the paddle length the light signals are measured by photomultiplier tubes (PMTs) at both ends of each paddle. The threshold of the TOF paddles is set to one-third of an MIP (energy loss of minimum-ionizing particles). Signals above the threshold are considered as TOF hits.

The time resolution of the TOF system is about 280 ps rms for BESS 93, which made it possible to separate the isotopes with rigidities up to 3 GV. This resolution assures no contamination from albedo particles. Both the top and bottom TOF counters provide ionization energy loss (dE/dx) measurements. With these redundant measurements, the misidentification of particles with charge $Z = +1$ and $Z = +2$ is less than 1%, and therefore is negligible.

2.1.5. *Intelligent Trigger System*

The BESS IDC and ODC provide the capability to determine the sign of particle rigidity and produce the track trigger on line. Because of the large geometric acceptance, and in order to save disk space for events with negative charge, the events with positive rigidity were selected with a prescaling countdown technique (see § 3.1 for details).

2.1.6. *Redundant Measurements*

At low energies, the velocity measured by the TOF counters and the rigidity measured by the magnet spectrometer can be cross-checked for different charged species.

The charge of an incident particle can be derived from the scintillator counters (both top and bottom TOF counters). Cross-checking with the ionization signals from the JET chamber, IDC, and ODC components ensures a very high certainty in charge identification.

The track positions in the r-ϕ plane and along the z-axis are measured by all four independent detectors: JET, IDC, ODC, and TOF. The redundant measurements in these detectors provide cross-checks of coordinates with the elongation of the track reconstructed in JET chamber. This helps select events with much more accurate rigidity measurement.

2.2. *BESS 93 Flight*

BESS had its first successful flight on 1993 July 26 from Lynn Lake, Manitoba, Canada, where the geomagnetic cutoff is 0.37 GV. The floating altitude was about 36.5 km (residual atmospheric depth of 5 g cm^{-2}), and the floating time was 17 hr. A total of 3.6 million events were recorded, from which about 1 million events were countdown data. This work, the analysis of hydrogen and helium energy spectra and their isotopic composition, is based on the countdown data.

3. ANALYSIS

3.1. *Trigger and Countdown Data*

BESS has two trigger levels: the TOF fast trigger (T0) and the negative track trigger (TT). Events with energy deposited in the top and bottom TOF above "low" (i.e., for $Z = 1$) or "high" (i.e., for $Z > 1$) thresholds will initialize the T0 trigger. The TT trigger is generated according to IDC/ODC hit pattern and is used to select events with negative curvature. The rate of T0 is several kilohertz, which is too high for the data-acquisition system. A countdown technique was used to reduce the rate of data recording; only one of 140 events passing the low T0 trigger and one of 40 events passing the high T0 trigger were processed and saved in the countdown data set. All events passing the T0 and TT triggers were saved.

The countdown data is an unbiased data set. We have used it in our data analysis to obtain the energy spectra of cosmic rays with positive charge.

3.2. *Events Selection*

There are 1,032,673 events in the countdown data set. After removing the events with negative velocity or negative rigidity, 552,454 events remained for this analysis.

3.2.1. *Single-Track Cuts*

Of the remaining events, only events with one, and only one, good track can be measured correctly. Single-track cuts were used to remove events not passing the fiducial region of the JET chamber or having nuclear interactions within the instrument materials. The single-track cuts include the criteria that:

1. There is only one good hit in each of the top and bottom TOF counters.
2. There is only one track in the JET chamber, and the track should have 10 or more hits in JET chamber.
3. The number of expected hits along the track in JET should be no less than 16.
4. The elongation of the track in the JET chamber should pass the fired counters in both the top and bottom TOF.

With the single-track cuts, about 20% of events were rejected because of multiple tracks in the JET chamber or multiple hits in the TOF counters. This corresponds to the fraction of events interacting in the spectrometer. See § 3.3. for details.

3.2.2. *Candidates for $Z = +1$ and $Z = +2$ Particles*

The charge identification was based on the ionization signals in both the top and bottom TOF scintillator counters. From the data set passing the single-track cuts, we selected the $Z = +1$ and $Z = +2$ particle candidates by applying a loose dE/dx cut (Fig. 2). The low solid curves in both Figures 2*a* and 2*b* show the upper limit used for the selection of $Z = +1$ particles. The regions defined by the pair of curves shown in Figures 2*a* and 2*b*, respectively, were used to select $Z = +2$ particles; 174,227 $Z = +1$ candidates and 47,310 $Z = +2$ candidates were selected at this stage.

3.2.3. *Track-Quality and Consistency Cuts*

In order to achieve good measurements of the rigidity, track-quality and consistency cuts were applied to the

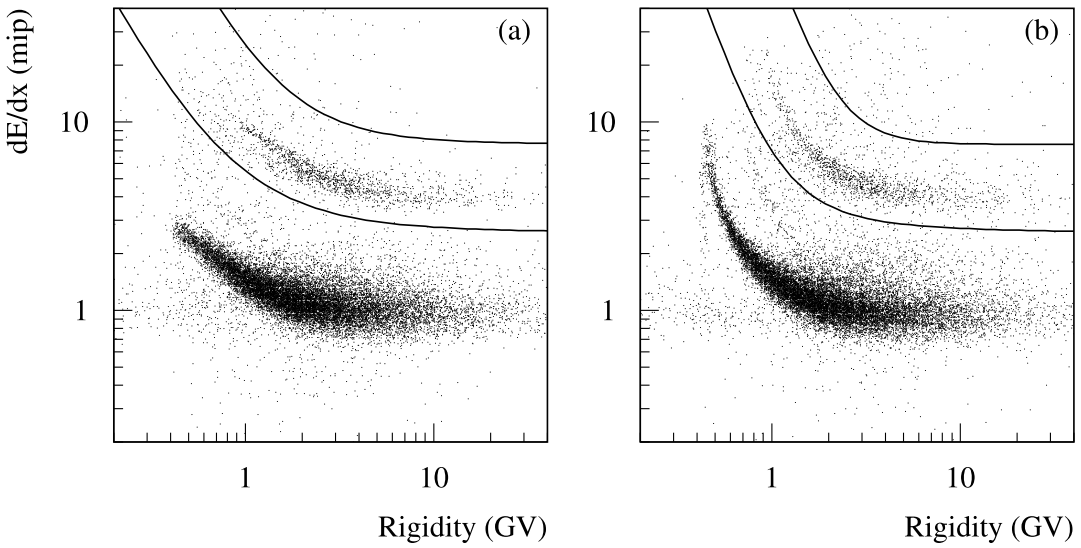

FIG. 2.—Ionization loss (dE/dx in mip, energy loss of minimum ionizing particles) in (*a*) the top scintillator counter and (*b*) the bottom scintillator counter vs. rigidity. The solid curves show the selection criteria for $Z = +1$ and $+2$ particles.

$Z = +1$ and $Z = +2$ candidates. The track-quality cuts were:

1. The number of central hits in JET ≥ 12. There are four sections in the JET chamber. The position measurement in the two side sections is less accurate than that in the central region because of the distortion of the electric field.
2. The number of hits associated with the r-ϕ fit ≥ 16. The accuracy of the track information depends on the number of hits used in the trajectory fitting.
3. The number of hits associated with the z fit ≥ 5.
4. The number of dropped hits (hits associated with the track but not used in the fit) ≤ 8. This cut rejects the events which do not have enough good hits for track fitting.
5. The number of extra hits (JET hits not concerned with the track) ≤ 20. This cut eliminates noisy events.
6. $\chi^2_{r\phi} < 4$, $\chi^2_z < 4$ (reduced χ^2 of fittings in the r-ϕ and r-z planes).

The consistency cuts ensure that the hits in the TOF and IDC are consistent with the JET track in both the r-ϕ and r-z planes. There are three consistency cuts shown below, where IDC1i/IDC2i and IDC1o/IDC2o represent the inner and outer layers of the top and bottom IDC, respectively, and TOFu and TOFl signify the upper and lower TOF, respectively. Delta represents their deviations from the JET measurements, and "min" selects the smaller parameter in the pair.

1. min ($\Delta r\phi_{\mathrm{IDC1}i}$, $\Delta r\phi_{\mathrm{IDC1}o}$) < 2.0 mm, min ($\Delta r\phi_{\mathrm{IDC2}i}$, $\Delta r\phi_{\mathrm{IDC2}o}$) < 2.0 mm.
2. min ($\Delta z_{\mathrm{IDC1}i}$, $\Delta z_{\mathrm{IDC1}o}$) < 2.0 mm, min ($\Delta z_{\mathrm{IDC2}i}$, $\Delta z_{\mathrm{IDC2}o}$) < 2.0 mm.
3. $|\Delta z_{\mathrm{TOF}u}| < 80.0$ mm, $|\Delta z_{\mathrm{TOF}l}| < 80.0$ mm.

Table 1 shows the number of events passing the above cuts and their corresponding efficiencies.

The efficiencies shown in Table 1 were used in the spectra normalization. Since the last consistency cut (TOF/JET Z consistency) presented a strong energy dependence on helium data at low energies (Fig. 3), an energy-dependent correction for efficiency was used for this particular case. The fact that more $Z = +2$ events at low energies were removed by this cut can be interpreted as strong Coulomb scattering by the low-energy $Z = +2$ particles (Reimer et al. 1998).

3.2.4. *Mass Measurement and Isotope Separation*

After performing the above data-selection procedure, we had two final data sets: one for $Z = +1$ and another for $Z = +2$. To achieve a pure hydrogen sample, the light particles, positrons, muons, and pions that survived the cuts had to be removed from the $Z = +1$ data set. Between the instrument cutoff (0.4 GV) and 1.4 GV, the time-of-flight measurement was used to identify these particles. Figure 4 shows the particle velocity measured by the TOF as a function of the rigidity measured by the MAG and JET. The solid curves represent the theoretical relation between velocity (β) and rigidity (R) for protons, ^{2}H, ^{3}H, ^{3}He, and

TABLE 1
EVENTS PASSING TRACK QUALITY AND CONSISTENCY CUTS

	Data Set			
	$Z = 1$		$Z = 2$	
Parameter	Events	Percentage	Events	Percentage
Candidates	174227	100	47310	100
Track Quality Cuts				
Central hits ≥ 12	169512	97.3	46123	97.5
r-ϕ fit ≥ 16	155911	89.5	42419	89.7
z fit ≥ 5	152963	87.8	41781	88.3
Dropped hits ≤ 8	144503	82.9	39557	81.5
Extra hits ≤ 20	144469	82.9	39542	83.6
$\chi^2_{r-\phi} < 4$, $\chi^2_z < 4$	135408	77.7	34591	73.1
Consistency Cuts				
IDC/JET r-ϕ cut	134276	77.1	34314	72.5
IDC/JET z cut	131248	75.3	33593	71.0
TOF/JET z cut	121846	69.9	29937	63.3

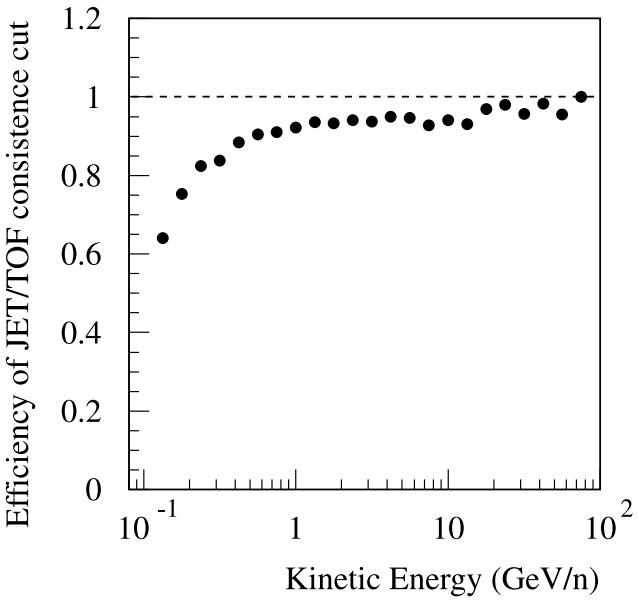

FIG. 3.—Energy dependence of the efficiency of the JET/TOF consistency cut for the $Z = +2$ data set.

^{4}He, respectively, which is

$$\beta = \left[1 + \left(\frac{mc^2}{ZR}\right)^2\right]^{1/2}. \quad (1)$$

The good agreement between the data and the theoretical prediction indicates that BESS 93 achieved a good measurement of both parameters.

Between 0.4 and 1.4 GV, the light particles $e^+/\mu^+/\pi^+$ could be clearly distinguished from hydrogen. The surviving fraction of $e^+/\mu^+/\pi^+$ was found to be 7% at 0.5 GV and 0.7% at 1.2 GV. Above 1.4 GV, no attempt was made to reject the light particles $e^+/\mu^+/\pi^+$ from hydrogen. The estimated light-particle contamination at float altitude at 1.5 GV was only about 0.5%, and the contamination decreases as the rigidity increases. Thus, we neglect this contamination at rigidities above 1.4 GV in our study.

In the rigidity interval from 0.4 to 3 GV, as shown in Figure 4, deuterons and ^{3}He can be separated from protons and ^{4}He in the BESS 93 experiment. To obtain separate energy spectra for different isotopes, mass histograms in different energy bins were used to separate the isotopes with a Gaussian fitting method (Seo et al. 1997a). Resulting spectra of protons, deuterons, ^{3}He, and ^{4}He are presented in § 4.2. For a comparison with other papers, in § 4.1 we show the hydrogen and helium energy spectra (particles/[m^2 sr s (GeV nucleon^{-1})]$^{-1}$) without isotope separation.

3.3. *Monte Carlo Simulation*

Monte Carlo simulations were essential for understanding the instrument performance and acceptance. Moreover, it was the only way to obtain the efficiency of the single-track cuts, since the incident cosmic-ray flux was unknown.

GEANT (Brun et al. 1984) is a powerful code for tracking and simulating interactions of protons. By using the GEANT simulation program, we set up the geometry configuration for BESS 93, which is shown Figure 1. Table 2 summarizes the detector elements and the material distribution along the vertical axis.

3.3.1. *Geometry Factor*

The geometry factor of the instrument is rigidity dependent, because the tracks of slow particles are more curved, and it is more likely that the slow particles do not pass through both the upper and lower TOF counters and the JET chamber. To account for this effect and the ionization energy-loss cutoff, the geometry factor was obtained by Monte Carlo simulation.

To test our simulation code, a geometric acceptance defined by only the top and bottom TOF counters was checked by two independent methods. In this simple case, it was possible to calculate the geometry factor by using a numerical integration calculation for relativistic particles. Both the numerical method and the simulation method gave the same result within 1% at energies above 2 GeV nucleon^{-1}.

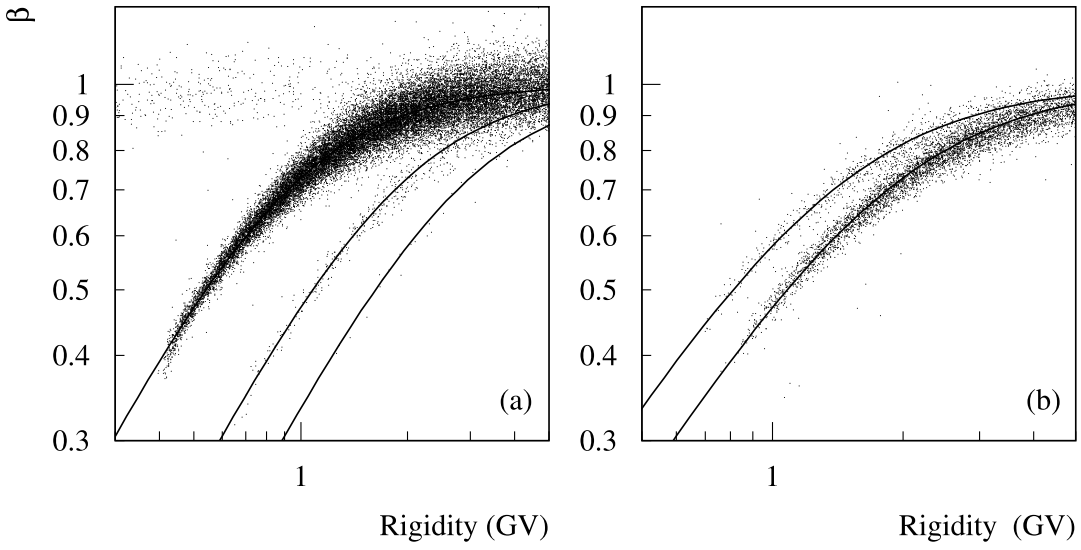

FIG. 4.—Velocity measured from the time of flight vs. rigidity for (*a*) $Z = +1$ and (*b*) $Z = +2$ particles. The solid curves show the theoretical relation between velocity and rigidity for protons, ^{2}H, ^{3}H, ^{3}He, and ^{4}He.

TABLE 2

BESS 93 Detector Elements and Material Distribution along Vertical Axis

Detectors	Thickness (g cm^{-2})	Material Composition
		Top Half
PV.....	0.67	Al (81%), CO_2 (19%)
TOF.....	2.2	SCN (94%), Al (6%)
ODC	0.76	Al (29%), epoxy (36%), Cu (17%), Mylar (18%)
MAG.....	4.7	Al (50%), Mylar (5%), Nb/Ti/Al/Cu/Malar (45%)
IDC	0.9	Al (30%), epoxy (31%), Cu (15%), Mylar (24%)
JET.....	0.17	Al (41%), epoxy (30%), Cu (29%)
		Bottom Half
JET.....	0.17	Al (41%), epoxy (30%), Cu (29%)
IDC	0.9	Al (30%), epoxy (31%), Cu (15%), Mylar (24%)
MAG.....	4.7	Al (50%), Mylar (5%), Nb/Ti/Al/Cu/Malar (45%)
ODC	0.76	Al (29%), epoxy (36%), Cu (17%), Mylar (18%)
TOF.....	2.2	SCN (94%), Al (6%)
PV.....	0.67	Al (81%), CO_2 (19%)

In order to match the procedure of our data selection, the geometry factor in this study was defined such that events within geometry could pass the single-track cuts when the physical processes were turned off. With this definition, one could easily determine the single-track cut efficiency due to nuclear interactions from Monte Carlo simulation.

In our analysis, 10^6 particles isotropically incident on BESS from the upper hemisphere were simulated for each energy bin (eight bins per decade). All physical processes were turned off, except for the ionization energy loss and the magnetic field, which decreased the geometry factor greatly at low energies. All events passing the single-track cuts were counted in the geometric factor calculation. Figure 5 shows the geometry factors for protons, deuterons, ^{3}He, and ^{4}He as a function of incident energy at the TOA. The instrument cutoff for different isotope species is clearly indicated in this figure. ^{3}He has the highest cutoff, around 0.2 GeV nucleon^{-1}. The energy dependence is less than 5% over the entire energy range above 0.2 GeV nucleon^{-1}, except for ^{3}He, which has a 10% drop at 0.2 GeV nucleon^{-1}. This energy dependence of the geometry factor was taken into account for calculation of the final energy spectra.

3.3.2. *Nuclear Interaction*

The most important requirement for determining the absolute fluxes is knowledge of the detector efficiencies. Particles with nuclear interactions inside the BESS instrument are likely to be removed by the single-track cuts. The single-track cut "efficiency" (fraction of particles not rejected) for nuclear interactions can be obtained from comparison of the simulated effective geometry factors with the pure geometry factors shown in § 3.3.1.

GEANT/GHEISHA was used directly for the proton simulation. Since GEANT does not accommodate simulation of heavy ions, we had to compile cross sections and find suitable hadron simulation packages that incorporate

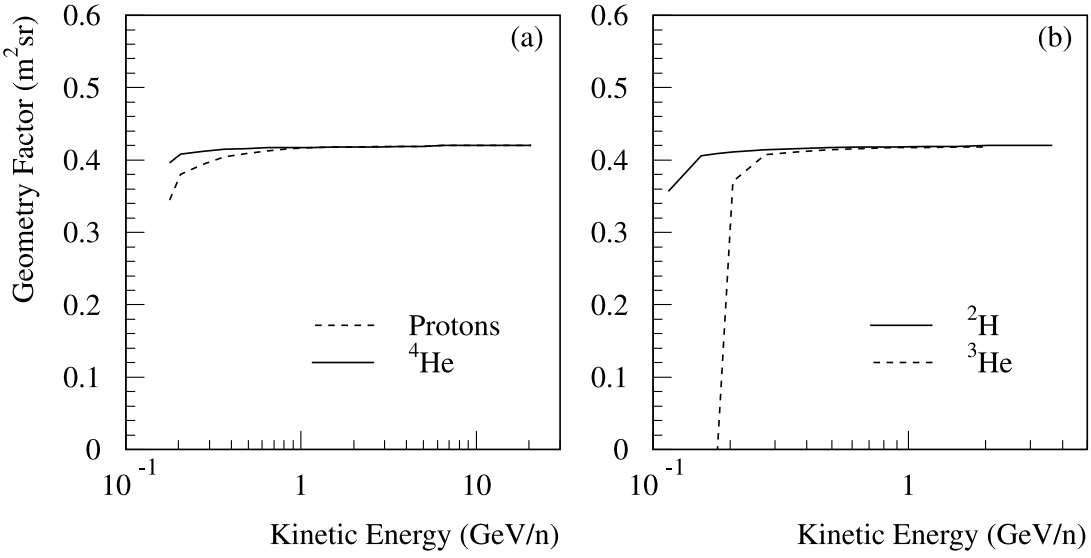

Fig. 5.—Geometry factors for protons, ^{2}H, ^{3}He, and ^{4}He vs. kinetic energy

detailed descriptions of various interactions of heavy ions. We have done an extensive search of the experimental cross section data for the interactions of deuterons and helium nuclei with different targets and compiled them to tune a parameter method for our heavy-ion simulations (see § 3.3.2.1 for details). We have adopted Kim's method (Kim et al. 1999) to interface GEANT with the hadronic simulation packages RQMD/FRITIOF. FRITIOF (Andersson et al. 1993) is based on semiclassical considerations of string dynamics for high-energy hadronic collisions. For energies in the center-of-mass frame less than 5 GeV nucleon^{-1}, relativistic quantum molecular dynamics (RQMD) was adopted for our simulations of heavy ions, deuterons, ^{3}He, and ^{4}He. RQMD is a semiclassical microscopic approach which combines classical propagation with stochastic interactions, and it describes the available single-particle spectra at the Alternating Gradient Synchrotron (AGS) and CERN successfully (Sorge 1995).

3.3.2.1. *Inelastic Cross Section*

Since there is a significant amount of material along the tracks of particles passing through the BESS instruments, the nuclear interaction loss significantly influences the detection efficiency, especially for the heavy nuclei. A typical incident particle that triggers the instrument has to traverse 5 g cm^{-2} of residual atmosphere plus the instrument materials (see Table 2 for details).

The most important input for the efficiency simulations was the inelastic cross sections of particles with the materials in the BESS instrument. Figure 6 shows that the nuclear inelastic cross sections of ^{4}He on hydrogen and carbon targets has a strong energy dependence below a few GeV nucleon^{-1}. Refer to Wang et al. (1999) for a discussion of the cross sections of hydrogen and helium isotopes, ^{2}H and ^{3}He.

A parameterization method was needed for calculating the cross section of a particle interacting with the different BESS materials at different energies. The Langley Research Center (LaRC) model, which was developed by Tripathi, Cucinotta, & Wilson (1996), was selected for our simulation study. It is a universal parameterization method for reaction cross sections, and it can be used for any system of colliding nuclei in the energy range from a few MeV nucleon^{-1} to a few GeV nucleon^{-1}. In the LaRC model, the reaction cross section σ_R can be expressed by the formula

$$\sigma_R = \pi r_0^2 (A_P^{1/3} + A_T^{1/3} + \delta_E)^2 \left(1 - \frac{B}{E_{\rm cm}}\right), \qquad (2)$$

where $r_0 = 1.1$ fm, A_p and A_t are the projectile and target mass numbers, respectively, and $E_{\rm cm}$ is the colliding system center-of-mass energy. The δ_E term represents two effects: transparency and Pauli blocking at intermediate and higher energies. The last term is the Coulomb interaction term, with B representing the energy dependent Coulomb barrier. We have compiled the experimental cross section data for deuterons and helium nuclei and used them to tune the LaRC model. As shown in Figure 6, the LaRC model calculations (*solid curves*) represent the cross section data very well.

The inelastic cross section becomes nearly constant above several GeV nucleon^{-1}. In order to cross-check our simulation results, the proton and ^{4}He interaction probabilities within the BESS instrument were also calculated using the proton nuclear cross section data provided in the particle properties data book (Montanet et al. 1994) and the ^{4}He nuclear cross section data compiled by Davis et al. (1995). Figures 7*a* and 7*b* show the inelastic cross sections as a function of atomic mass number of the target nuclei for protons and ^{4}He, respectively.

These cross sections were parameterized by using the formulas

$$\sigma_{p+A} = 40 A^{0.71} \text{ (mb)}, \qquad (3)$$

$$\sigma_{^4\text{He}+A} = (5.69 + 6.58\ A^{0.355})^2 \text{ (mb)}. \qquad (4)$$

The solid curves shown in Figure 7 reflect the above parameterizations. Based on the cross section data, we calculated

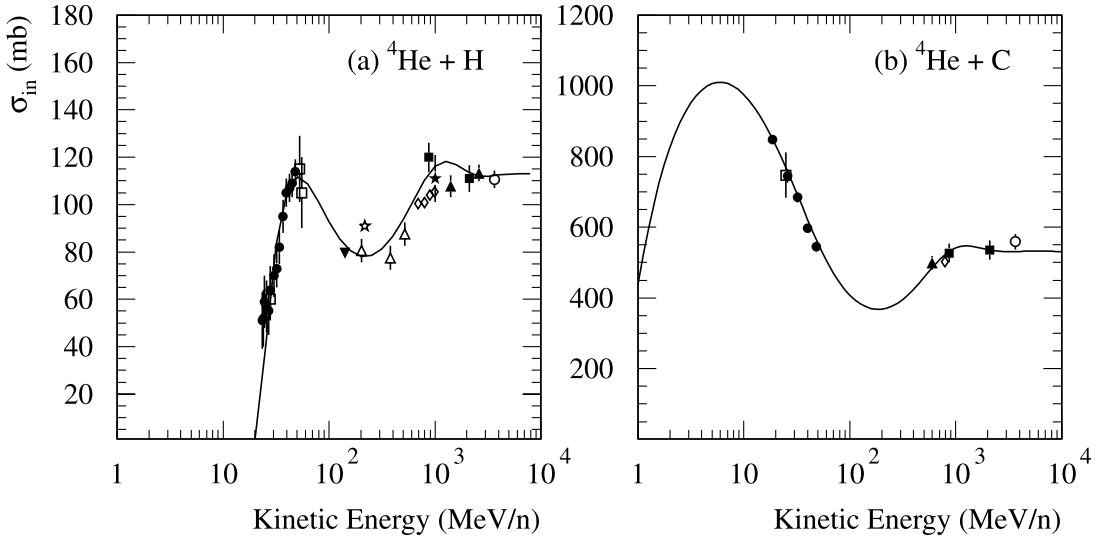

FIG. 6.—Inelastic cross section of ^{4}He on (*a*) hydrogen and (*b*) carbon targets with the LaRC parameterization. Data points in plot (*a*) are as follows: *filled circles*: Carlson (1996); *open squares*: Meyer (1972); *filled downward-pointing triangle*: Nicholls et al. (1972); *open star*: Abdullin et al. (1992); *open triangles*: Webber (1997); *diamonds*: Velichko et al. (1985); *filled squares*: Jaros et al. (1978); *filled star*: Igo et al. (1967); *filled triangles*: Glagolev et al. (1993); *open circle*: Ableev et al. (1985). Data points in plot (*b*) are as follows: *filled circles*: Auce et al. (1994); *open square*: Dubar et al. (1989); *filled triangles*: Webber et al. (1990); *diamond*: Tanihata et al. (1985); *filled squares*: Jaros et al. (1978); *open circle*: Ableev et al. (1985).

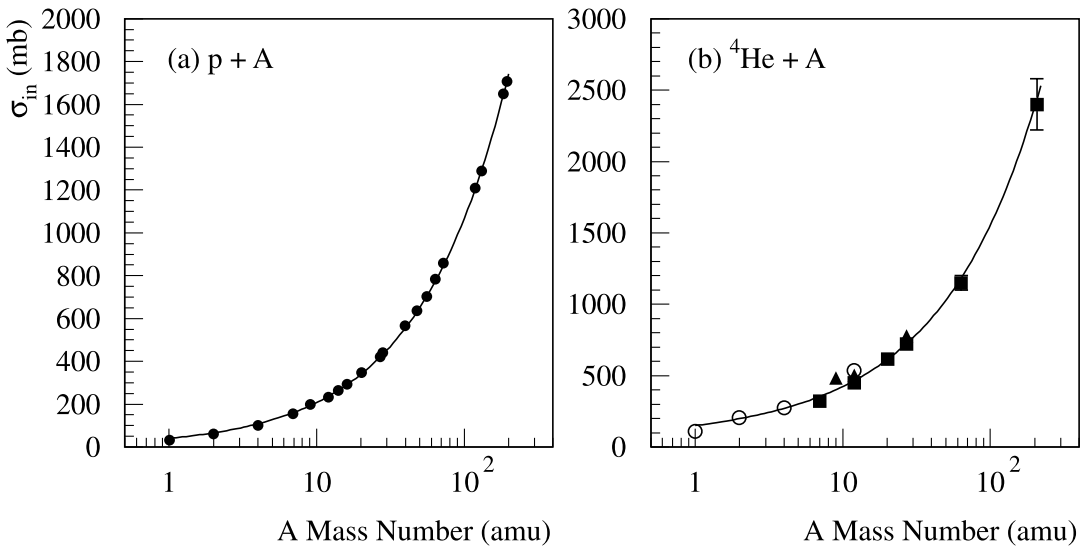

FIG. 7.—Inelastic cross section of (*a*) protons and (*b*) ^{4}He as a function of the target mass number. The solid curves show a best fit. Data points are as follows: *filled circles*: Montanet (1994); *open circles*: Jaros et al. (1978); *filled square*: Aksinenko et al. (1980); *filled triangles*: Tanihata et al. (1985).

the mean free path of protons and ^{4}He in air to be 89.9 and 46.6 g cm^{-2}, respectively. These are consistent with the value of 90 and 45 g cm^{-2} used in other papers (Rygg & Earl 1971; Hernandez et al. 1990; Papini et al. 1993a; Wefel et al. 1995b).

3.3.2.2. *Proton Interaction Efficiency*

In a complete simulation with all physical processes on, we obtained the proton detection "efficiency" (noninteraction fraction). The dashed curve in Figure 8*a* shows our simulation results. This efficiency shows a slight energy dependence due to the energy-dependent cross section of $p + A$ interaction.

The purpose of the single-track cuts was to remove events with multiple tracks. The track identification power of the JET chamber and the fine-segmented TOF counters ensure that most events with interaction above the bottom TOF counters will be rejected. Based on the geometric acceptance defined in § 3.3.1, the efficiency for normalization due to nuclear interaction is about 0.80 at energies above 5 GeV.

3.3.2.3. *Interaction Efficiency for Heavier Nuclei*

To adopt GEANT for heavy-ion simulations, two interfaces were made. One was to implement the LaRC model in determining the interaction probabilities for heavy ions, and another was to embed RQMD/FRITIOF into GEANT, in order to perform the heavy-ion simulation.

With the enhanced code, we calculated the effective geometry factors for deuterons, ^{3}He, and ^{4}He. By comparison with the pure geometry factors presented in Figure 5, we obtained the detection efficiency (noninteraction fraction) of inelastic interactions. The energy-dependent efficiencies for hydrogen, helium, and their isotopes are shown in Figure 8. Over the entire energy range (0.2–10 GeV nucleon^{-1}), the detector efficiency changes about 8%

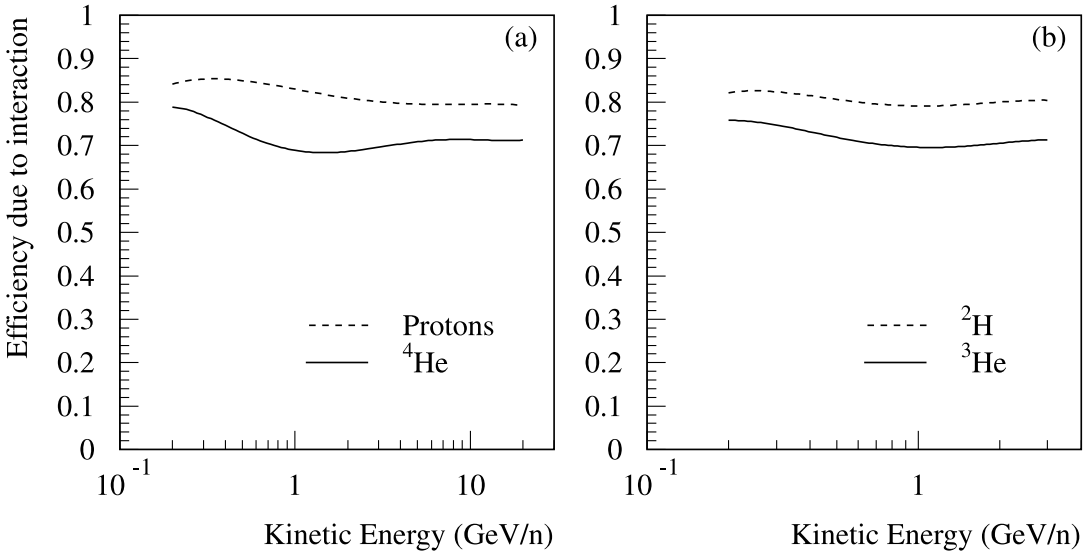

FIG. 8.—Efficiency due to nuclear interactions for protons, ^{2}H, ^{3}He, and ^{4}He vs. kinetic energy

and 15% for protons and ^{4}He, respectively. At high energies ($\geq$5 GeV nucleon^{-1}), similar to protons, the efficiency of ^{4}He becomes almost constant, with a value of 70%.

An independent check was done with the cross-section data shown in Figure 7. The strong identification capability of the BESS instrument for multiple tracks and multiple hits allowed rejection of most of the events that interacted above the bottom TOF counters by the single-track cuts. Based on the parameterized cross section in equations (3) and (4) and the material distribution shown in Table 2, we could calculate the noninteraction probability for particles passing through all material above the bottom TOF counters. For an average incident zenith angle of 24° (see § 3.4.1), the noninteraction probability along the vertical axis down to the bottom TOF counters is 82% and 70% for protons and ^{4}He, respectively. This alternative calculation confirmed our simulation results. The simulated proton efficiency was slightly low, less than 3% at high energies, because elastic interactions were taken into account in the GHEISHA proton simulations.

3.3.2.4. *δ-Ray Effect*

The δ-ray is the energetic knock-on electron; its production is proportional to the square of the primary particle charge, and its maximum energy is proportional to the primary particle energy. Therefore, there is a high probability that high-energy good events will fail the single-track cuts because of the δ-ray effect. BESS has the finest segmentation in different detector components among similar balloon-borne magnet spectrometers. The δ-ray effect was demonstrated to significantly influence the single-track cut efficiencies for the high-charge and high-energy measurements in BESS (Seo et al. 2000).

During the ionization process, energetic electrons are knocked out. For primary particles with momentum $M\beta\gamma$ less than 100 GeV/c nucleon^{-1}, the maximum energy of produced δ-rays can be given approximately by

$$E_{\delta,\max} = 2m_e c^2 \beta^2 \gamma^2 \ . \quad (5)$$

For 1 GeV protons, $E_{\delta,\max}$ is 3.4 MeV. In order to study the δ-ray effect and make the corresponding correction in the data analysis, the δ rays were simulated explicitly with a threshold of 100 keV, based on the GEANT code. The typical penetration range of 100 keV electrons is only 0.014 g cm^{-2} in common materials (e.g., 0.1 mm in scintillator), and its cyclotron radius in a 1 Tesla magnetic field is only 1 mm. The simulation indicates that the influence of electrons with energy of 100 keV or less is negligible.

Figure 9 shows the efficiency for good events passing the single-track cuts when the δ-ray effect is taken into account explicitly. There is no significant difference between isotopes. Therefore, the results are presented only for $Z = +1$ and $Z = +2$ particles, respectively. We find that the correction due to δ-rays for $Z = +2$ is up to 15% around 10 GeV nucleon^{-1}, which is significant.

In general, the ionization energy loss (dE/dx) of particles in the scintillator counters agrees with a Landau distribution. To separate $Z = +1$ particles from $Z = +2$ particles, one can set a dE/dx cut around 2.5 MIPs. Because of the long Landau tail, according to simulation, about 3% or 6% of $Z = +1$ particles could be removed by a single cut or a pair of dE/dx cuts, respectively.

Since the energetic δ-rays produced in the ionization process may have a high probability to escape the sensitive detector volume, the actual ionization energy deposit distribution of primary particles in the 2 cm TOF counters has a much shorter tail than the Landau distribution. Our simulation studies indicated that if the δ-ray effect is taken into account, the loose dE/dx cuts to select $Z = +1$ and $Z = +2$ candidates shown in Figure 2 have almost 100% selection efficiency.

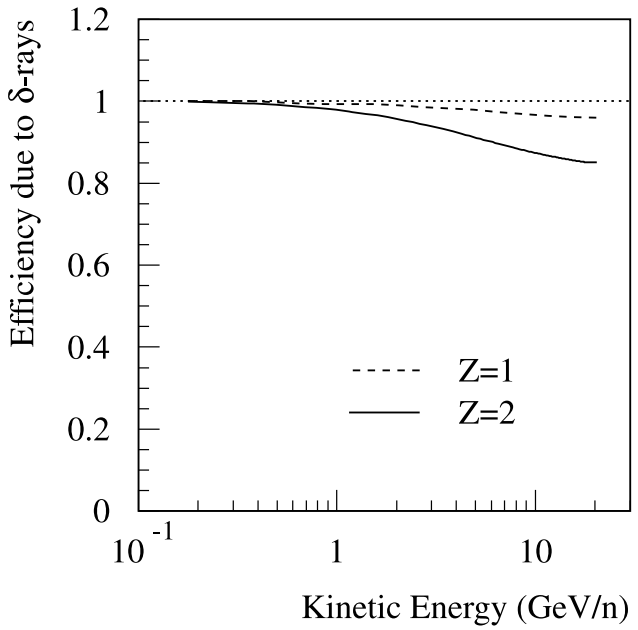

FIG. 9.—Efficiency due to δ-ray effect for $Z = +1$ (*dashed curve*) and $Z = +2$ (*solid curve*) events vs. kinetic energy.

Further simulation studies showed that about 4% of the events that passed the single-track cuts did not pass the loose dE/dx cuts shown in Figure 2. With a detailed check, we found that the dE/dx cuts remove events that have nuclear interactions inside the TOF counters. In some nuclear interactions, only the particle neutron number is changed and no charged secondary is created. Although those events interacted with the scintillator counters, they still passed the single-track cuts because either no charged secondary was produced or charged secondaries did not pass the other sensitive detector components. Obviously, we had to make efficiency corrections for the dE/dx cuts, and we have included them in the interaction efficiency corrections discussed in this section.

3.4. *Atmosphere Corrections*

Because of the influence of the atmospheric overburden, the spectra measured at balloon altitudes are not the same as the primary cosmic-ray spectra at the TOA. The spectra are modified by the ionization process at low energies and by the loss of particles from interactions at all energies. Secondary particles are also produced in the interactions of cosmic rays with air nuclei targets. We discuss these aspects below in detail.

3.4.1. *Ionization Energy Loss*

A cosmic-ray particle that traverses from the TOA and triggers the BESS instrument will lose energy both in the atmosphere and in the materials of the BESS instrument. The combined energy loss has a significant effect on the

energy bins at low energies. Two methods were used to make corrections for the ionization energy loss, and they can be cross-checked with each other.

A simple approach is to integrate the average energy loss along a typical trajectory and make a table corresponding to the kinetic energy bins at the TOA and the rigidity bins at BESS/JET. The energy loss of particles traversing through depth x is

$$\Delta E(x) = \int_0^x \frac{dE}{dx}\, dx\,, \tag{6}$$

where dE/dx is the stopping power. For protons, we used data from the *Tables of Energy Losses and Ranges of Heavy Charged Particles* (Barkas & Berger 1964). For heavier ions, the stopping power as a function of kinetic energy per nucleon was scaled from the proton data according to

$$\left|\frac{dE}{dx}\right|_{(Z,A)} = \left|\frac{dE}{dx}\right|_{(1,1)} \frac{z^2}{A}\,. \tag{7}$$

A more accurate method is to make event-by-event corrections according to the actual trajectory. The actual thickness of the atmosphere and instrument materials traversed by a particle depends on the inclination of the particle trajectory. The trajectory of a good event can be precisely reconstructed in the BESS experiment, so it could then be extrapolated to the TOA according to its zenith elevation and azimuth angles. The utility routines of GEANT were used to calculate the event-by-event energy-loss fraction along the trajectory, and this latter method was used in this study.

The results of both methods are presented in Figure 10. The dots show the BESS data with the kinetic energy at the TOA corrected with the second method. As expected, the numerical calculation with a zenith angle of 0° corresponds to the minimum energy-loss correction (*dashed curves*). The solid curve in Figure 10 represents the numerical calculation with a zenith angle of 24°, which indicates that the selected BESS events had an average zenith angle close to 24°. This value was used in the instrument efficiency estimate and atmosphere attenuation calculation in this study. If we neglect the influence of the inclination angle, which is a common procedure used by other authors, it will lead to an undercorrection of about 8 MeV for protons at the BESS instrument cutoff (180 MeV). As the energy increases, the difference becomes rapidly small and hence negligible.

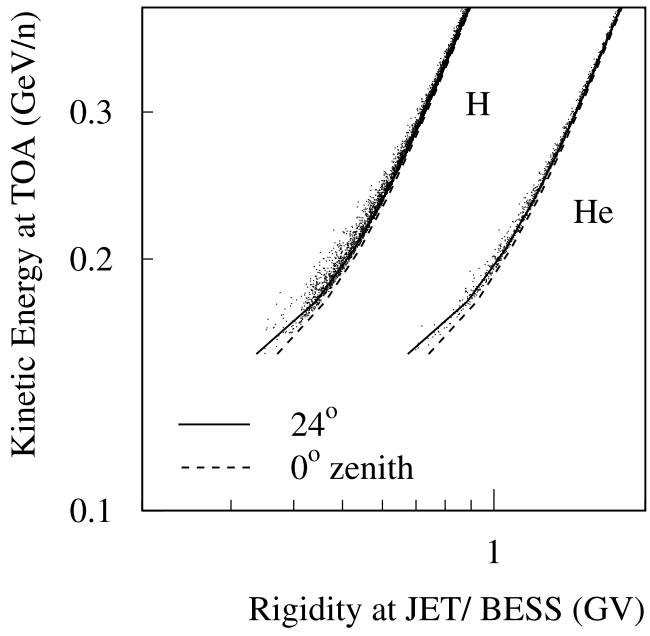

FIG. 10.—Corrected kinetic energy at TOA vs. rigidity measured by BESS. The curves represent numerical calculations with zenith angles of 0° (*dashed curves*) and 24° (*solid curves*).

3.4.2. *Atmosphere Attenuation*

Primary cosmic rays are lost in the atmosphere because of inelastic nuclear interactions with the air target nuclei. The amount of residual atmosphere above the instrument was taken to be 5.0 ± 0.2 g cm^{-2}. The probabilities for hydrogen, helium, and their isotopes surviving after traversing the residual atmosphere were also calculated using the adaptive GEANT code for a inclination angle of 24°. Particles that underwent inelastic nuclear interactions in the simulation were assumed to go undetected.

Table 3 shows the simulation results at 5 GeV nucleon^{-1}. There is a slight energy dependence, about 2% for protons and deuterons and about 4% for ^{3}He and ^{4}He. In our spectra normalization, the energy-dependent efficiencies were used. Using the mean free path value derived for protons and ^{4}He in § 3.3.2, we can calculate the noninteraction probabilities in the residual atmosphere. We got exactly the same values with both methods, which are shown in Table 3.

3.4.3. *Corrections for Secondaries*

In the balloon-borne experiments, secondary particles produced in the air will be measured along with the primary cosmic rays. Therefore, the corrections for secondary particles become very important for determining the cosmic-ray spectra at the TOA, especially for the light elements, protons and deuterons, at low energies.

Secondary corrections are sensitive to the flux of major primaries (protons and ^{4}He, etc.). The spectra of primaries measured by BESS 93 were used for self-consistency in this calculation. The secondary particle flux $J(E, x)$ was evaluated according to the transport equation

$$\frac{\partial J(E, x)}{\partial x} = \frac{\partial}{\partial E}\left[J(E, x)\frac{dE}{dx}\right] - \frac{J(E, x)}{\lambda(E)} + P(E, x)\,. \tag{8}$$

Three physical processes were taken into account, i.e., ionization, attenuation, and production, which are represented by the three terms on the right-hand side, respectively. Secondary sources of particles include (1) spallation of cosmic-ray nuclei, (2) evaporation and recoil nucleons from air target nuclei, and (3) high-energy interactions. Secondary protons and deuterons come from all three sources, while secondary ^{3}He is mainly produced in the spallation of heavy nuclei. The Runge-Kutta technique was used to solve

TABLE 3

ATTENUATION CORRECTION EFFICIENCIES η IN THE BESS 93 RESIDUAL ATMOSPHERE OF 5 G cm^{-2} AT 5 GeV NUCLEON^{-1}

Particles	Proton	Deuteron	^{3}He	^{4}He
η	0.94	0.92	0.88	0.89

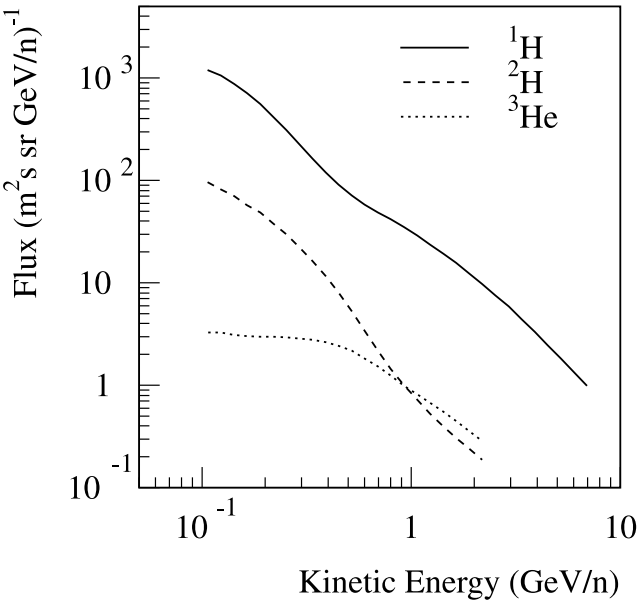

FIG. 11.—Flux of secondary particles at BESS 93 flight duration. The solid, dashed, and dotted curves, respectively, represent secondary protons, ^{2}H, and ^{3}He produced in the residual atmosphere above the instrument.

equation (8) numerically (Papini et al. 1993a, 1993b, 1993c, 1996).

The calculated secondary proton, deuteron, and ^{3}He flux corresponding to BESS 93 are presented in Figure 11. The flux of secondary protons and deuterons is much higher than that of ^{3}He at low energies, where the main contribution comes from the recoil and evaporation of air target nuclei. The differential cross section of secondary production for this process depends strongly on the mass and charge numbers of the produced particles. There is a large contribution to secondary protons from higher energy cosmic-ray protons slowing down as a result of inelastic interactions. Compared with the flux of the primary particles presented in § 4.2, the secondary correction is about 42% and 63% for protons and deuterons, respectively, around the lowest measured energy (0.2 GeV nucleon^{-1}). This correction decreases rapidly with increasing energy. It becomes less than 4% for protons at energies above 1 GeV nucleon^{-1}, and about 12% for deuterons at the highest measured energy, 0.75 GeV nucleon^{-1}.

3.5. *Normalization*

The count spectra $N(E)$ of selected hydrogen, helium, and their isotopes were normalized to obtain the final energy spectra. The differential fluxes at the TOA as a function of kinetic energy per nucleon, E, are given by

$$F_{\rm TOA}(E) = \left[\frac{N(E)C_d}{G(E)\varepsilon_i(E)\varepsilon_c(E)T\Delta E_{\rm in}} - f_{\rm sec}(E)\right]\frac{\Delta E_{\rm in}}{\eta(E)\Delta E_{\rm TOA}}, \quad (9)$$

where C_d is the inverse of the countdown rate (140 for $Z = +1$, 40 for $Z = +2$), $G(E)$ is the geometry factor (0.42 m^2 sr at high energies; the energy dependence is shown Fig. 5), $\varepsilon_i(E)$ is the detection efficiency for nuclear interactions and the δ-ray effect presented in Figures 8 and 9, $\varepsilon_c(E)$ is the efficiency of the data-selection cuts (see Table 1), T is the live time (72.4% live fraction of 42,389 s), $\Delta E_{\rm in}$ is the bin size inside BESS and corresponds to $\Delta E_{\rm TOA}$ at the TOA, $\eta(E)$ is the correction factor of attenuation loss, and $f_{\rm sec}(E)$ is the atmospheric secondary spectra calculated for BESS 93 (Fig. 11).

3.6. *Uncertainty Estimate*

Following our normalization procedure, we could estimate the uncertainties of our final results. The following uncertainties were considered in our analysis:

The statistical error was considered for the events counts. Since the counts for deuterons and ^{3}He isotopes were obtained from a double-Gaussian fit, another energy-dependent uncertainty was introduced at higher energies in the measured range.

The geometry factor calculated in the GEANT simulation has a good precision; it was cross-checked with the numerical method, whose uncertainty is less than 1%.

The uncertainty due to correction for nuclear interactions is isotope dependent, and it is mainly related to the inelastic cross section data and the BESS material distribution. Assuming an uncertainty of 5% in the cross sections used for protons and 10% each for deuterons, ^{3}He, and ^{4}He, and a 10% uncertainty in the material thickness, the results show a systematic error on the final spectra of 3% for protons, 4% for deuterons, and 6% for helium nuclei. Similar consideration was applied to η for the atmosphere

TABLE 4

SUMMARY OF NORMALIZATION PARAMETER UNCERTAINTIES

	PARTICLES			
PARAMETER	Proton % (GeV nucleon^{-1})	Deuteron % (GeV nucleon^{-1})	^{3}He % (GeV nucleon^{-1})	^{4}He (%)
Geometry factor	1	1	1	1
Attenuation in air	1	1	1	1
Interaction	3	4	6	6
Secondary correction.....	15 (0.2)	34 (0.2)	3 (0.22)	
	5 (0.3)	20 (0.3)	3 (0.3)	
	2 (0.5)	8 (0.4)	2 (0.6)	
	1 (1)	3 (0.65)	1.5 (1)	
		9 (0.48)	6 (0.65)	
Gaussian fit		15 (0.65)	8 (0.87)	
			13 (1.2)	

attenuation correction, but the systematic error of η is much smaller.

A difference of up to 40% or larger exists among the different secondary calculations (Rygg & Earl 1971; Webber et al. 1991; Wefel et al. 1995b; Papini et al. 1993a, 1993b, 1993c, 1996). Although the primary spectra obtained in this experiment were used in our secondary calculation, to be conservative, a $\pm 20\%$ uncertainty in secondary corrections was assumed in this study. While the influence on the results is negligible ($<1\%$) at energies above 1 GeV nucleon^{-1}, it is the dominant uncertainty at the lowest measured energies, where the systematic error due to atmospheric secondaries can be up to 15% and 35%, respectively, for proton and deuteron spectra at 0.2 GeV nucleon^{-1}.

Table 4 summarizes the uncertainties of all the parameters used in the normalization of our final energy spectra.

4. RESULTS

The procedures discussed above were used to obtain the BESS 93 fluxes. The results include the energy spectra of cosmic-ray hydrogen, helium nuclei, and their isotopes at the TOA, as well as the isotope ratios of ^{2}H/^{1}H, ^{2}H/^{4}He, and ^{3}He/^{4}He. We present the hydrogen and helium energy spectra from the lowest measured energy (0.2 GeV nucleon^{-1}) up to 10 GeV nucleon^{-1}. In this section, we compare our results with both other experimental measurements and available calculated spectra. The uncertainties for all results are estimated.

4.1. *Absolute Flux of Hydrogen and Helium*

The absolute fluxes of BESS 93 hydrogen (protons including deuterons) and helium (^{4}He including ^{3}He) extrapolated to the TOA are given in Tables 5 and 6. For comparison with other experimental data, the statistical error and the systematic error are presented separately. The TOA spectra are shown in Figure 12 along with the measurements from other balloon and satellite experiments about the same time. Only statistical errors are shown with error bars in the figure, and except for the lowest energy of *IMP-8* data and Alpha Magnetic Spectrometer (AMS) data, they are all equal to or smaller than the plot symbols. It should be noted that the low-energy BESS 93 data are very consistent with the *IMP-8* satellite data measured for a similar time period (1993 July 14–August 9). At higher energies, the BESS 93 spectra are very consistent with the spectra measured in the successive years (IMAX-92 and CAPRICE-94), after taking into account the corresponding levels of solar modulation.

The overall uncertainty of the hydrogen spectrum is about 4%, except at low energies, where it can be up to 15% due to secondary corrections. The total uncertainty of the helium spectrum, which is mainly deduced from the nuclear interaction correction, is about 7% over the entire measured energy range. The total error bars, including statistical error and systematic error, is equal to or smaller than the symbol size, except for the lowest proton point, for which the total error bar is slightly larger than its symbol.

4.2. *Energy Spectra of Protons, Deuterons,* ^{3}He, *and* ^{4}He *at TOA*

Isotopes were separated up to 3 GV rigidity from the mass histograms by using double Gaussian fitting. Figure 13 and Tables 5, 6, 7, and 8 show the separate energy spectra of protons, deuterons, ^{3}He, and ^{4}He with kinetic energies up to about 1 GeV nucleon^{-1}. Only statistical errors are shown with error bars in the figure. Previous measurements of deuterons and ^{3}He at low energies are shown for comparison. IMAX provided deuteron and ^{3}He measurements, but under stronger solar modulation (de Nolfo et al. 2000; Menn et al. 2000) for a similar energy range. The IMAX deuteron fluxes seem to be somewhat higher than what is expected according to the solar modulation level determined by their proton and helium measurements. Our BESS 93 measurement is the first one obtained close to a solar minimum.

The overall uncertainties of protons and ^{4}He are similar to those of hydrogen and helium discussed above. The total uncertainty of the deuteron flux is about 20% but goes up to 42% at the lowest energy, primarily due to the large fraction of secondary corrections. The overall uncertainty of ^{3}He is about 10%, except for the lowest (0.2 GeV nucleon^{-1}) and highest (1.2 GeV nucleon^{-1}) energies, where the uncertainties are about 16% due to the statistical

TABLE 5

BESS 93 Proton and Hydrogen Fluxes at the Top of the Atmosphere

Kinetic Energy (GeV)		Proton Flux at TOA[a]	Hydrogen Flux at TOA[a]
Interval	Mean	(m^2 s sr GeV)$^{-1}$	(m^2 s sr GeV)$^{-1}$
0.18–0.24.....	0.21	$(1.04 \pm 0.03 \pm 0.15) \times 10^3$	$(1.05 \pm 0.03 \pm 0.15) \times 10^3$
0.24–0.32.....	0.27	$(1.26 \pm 0.02 \pm 0.09) \times 10^3$	$(1.27 \pm 0.02 \pm 0.09) \times 10^3$
0.32–0.42.....	0.37	$(1.32 \pm 0.02 \pm 0.06) \times 10^3$	$(1.33 \pm 0.02 \pm 0.06) \times 10^3$
0.42–0.56.....	0.49	$(1.23 \pm 0.01 \pm 0.05) \times 10^3$	$(1.25 \pm 0.01 \pm 0.05) \times 10^3$
0.56–0.75.....	0.65	$(1.09 \pm 0.01 \pm 0.04) \times 10^3$	$(1.11 \pm 0.01 \pm 0.04) \times 10^3$
0.75–1.00.....	0.87	$(9.02 \pm 0.09 \pm 0.33) \times 10^2$	$(9.21 \pm 0.09 \pm 0.33) \times 10^2$
1.00–1.33.....	1.15	$(7.14 \pm 0.07 \pm 0.26) \times 10^2$	$(7.32 \pm 0.07 \pm 0.26) \times 10^2$
1.33–1.78.....	1.54	$(5.32 \pm 0.05 \pm 0.19) \times 10^2$	$(5.41 \pm 0.05 \pm 0.19) \times 10^2$
1.78–2.37.....	2.05	$(3.75 \pm 0.04 \pm 0.13) \times 10^2$	$(3.81 \pm 0.04 \pm 0.13) \times 10^2$
2.37–3.16.....	2.74		$(2.48 \pm 0.03 \pm 0.09) \times 10^2$
3.16–4.22.....	3.65		$(1.56 \pm 0.02 \pm 0.05) \times 10^2$
4.22–5.62.....	4.87		$(8.71 \pm 0.12 \pm 0.30) \times 10^1$
5.62–7.50.....	6.49		$(5.06 \pm 0.08 \pm 0.17) \times 10^1$
7.50–10.0.....	8.66		$(2.78 \pm 0.05 \pm 0.09) \times 10^1$

[a] Top of the atmosphere; the quoted errors include two parts: the statistical error and the systematic error.

TABLE 6

BESS 93 ^{4}He and Helium Fluxes at the Top of the Atmosphere

Kinetic Energy (GeV nucleon^{-1})		^{4}He Flux at TOA[a]	Helium Flux at TOA[a]
Interval	Mean	(m^2 s sr GeV nucleon^{-1})$^{-1}$	(m^2 s sr GeV nucleon^{-1})$^{-1}$
0.18–0.24	0.21	$(1.54 \pm 0.05 \pm 0.10) \times 10^2$	$(2.08 \pm 0.06 \pm 0.13) \times 10^2$
0.24–0.32	0.27	$(1.70 \pm 0.04 \pm 0.10) \times 10^2$	$(2.15 \pm 0.05 \pm 0.13) \times 10^2$
0.32–0.42	0.37	$(1.71 \pm 0.04 \pm 0.11) \times 10^2$	$(2.07 \pm 0.04 \pm 0.13) \times 10^2$
0.42–0.56	0.49	$(1.45 \pm 0.03 \pm 0.09) \times 10^2$	$(1.71 \pm 0.03 \pm 0.10) \times 10^2$
0.56–0.75	0.65	$(1.13 \pm 0.02 \pm 0.07) \times 10^2$	$(1.32 \pm 0.02 \pm 0.08) \times 10^2$
0.75–1.00.....	0.87	$(8.75 \pm 0.17 \pm 0.54) \times 10^1$	$(1.02 \pm 0.02 \pm 0.06) \times 10^2$
1.00–1.33.....	1.15	$(5.84 \pm 0.12 \pm 0.36) \times 10^1$	$(6.73 \pm 0.13 \pm 0.42) \times 10^1$
1.33–1.78.....	1.54		$(4.45 \pm 0.09 \pm 0.27) \times 10^1$
1.78–2.37.....	2.05		$(2.82 \pm 0.06 \pm 0.17) \times 10^1$
2.37–3.16.....	2.74		$(1.77 \pm 0.04 \pm 0.11) \times 10^1$
3.16–4.22	3.65		$(9.68 \pm 0.28 \pm 0.60) \times 10^0$
4.22–5.62.....	4.87		$(5.65 \pm 0.18 \pm 0.35) \times 10^0$
5.62–7.50.....	6.49		$(2.97 \pm 0.12 \pm 0.18) \times 10^0$
7.50–10.0.....	8.66		$(1.65 \pm 0.07 \pm 0.10) \times 10^0$

[a] Top of the atmosphere; the quoted errors include two parts: the statistical error and the systematic error.

and Gaussian fit uncertainties. In Figure 13, the overall uncertainties for the deuteron spectrum are indicated by the shaded region, while the overall uncertainties for other spectra are equal to or smaller than the symbol size.

The curves in Figure 13 represent expected spectra from two propagation models. The solid curves are for a reacceleration model and the dashed curves are for a standard leaky-box model (SLBM).

A single power-law escape length $\lambda_e = 14R^{-1/3}$ g cm^{-2} (Seo & Ptuskin 1994) was used in the reacceleration model calculation. For the source spectra, a power law in rigidity with spectral index of 2.4 was assumed for each species. For each isotope, the local interstellar spectrum obtained from the Galactic propagation calculation was subjected to solar modulation based on a numerical solution for a spherically symmetric model (Fisk, Forman, & Axford 1973) including diffusion, convection, and adiabatic deceleration. Our resulting spectra are consistent both with previous observations at low energies during solar minimum periods and with spectra calculated with the modulation parameter 700 MV. The calculated spectra of the SLBM with the modulation parameter 600 MV gives the best fit to the data for all four isotope components, as shown by the dashed curves in Figure 13 (Seo et al. 1994). The parameters for these models

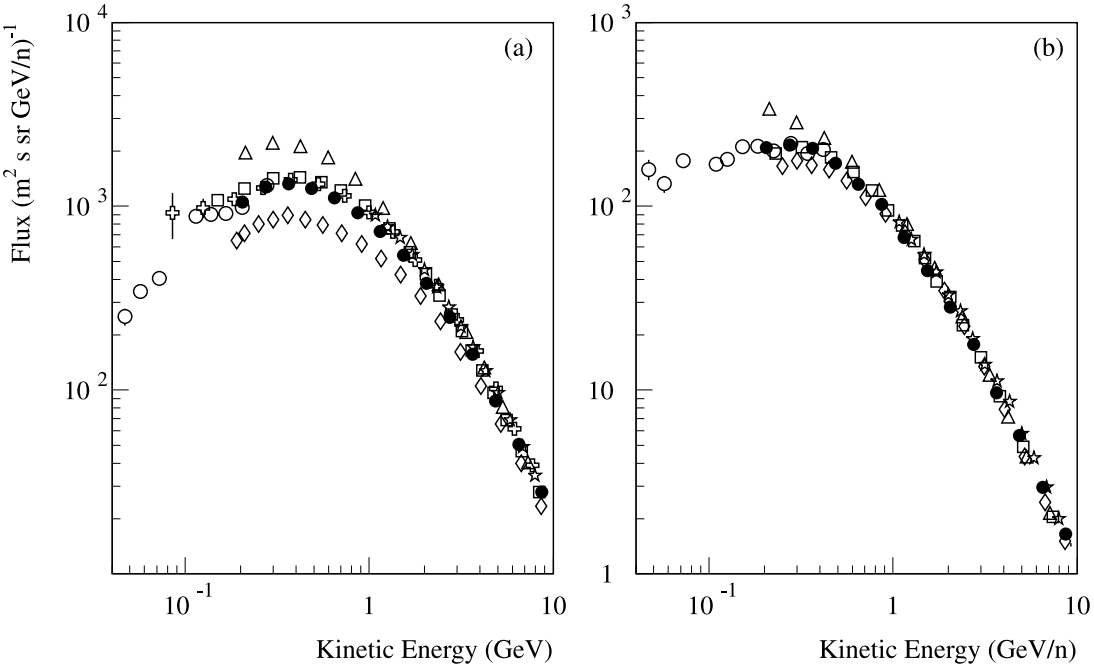

Fig. 12.—BESS 93 absolute fluxes vs. kinetic energy per nucleon at the top of atmosphere for (*a*) hydrogen and (*b*) helium, compared to other recent balloon and space measurements. The data points are as follows: *filled circles*: this work; *open circles*: *IMP-8* data (1993 July 14-August 9); *triangles*: LEAP 87 measurements (solar minimum, Seo et al. 1991); *diamonds*: IMAX 92 measurements (Menn et al. 2000); *squares*: CAPRICE 94 measurements (Boezio et al. 1999); *stars*: BESS 98 measurements (Sanuki et al. 2000); *crosses*: AMS 98 measurements (Alcaraz et al. 2000).

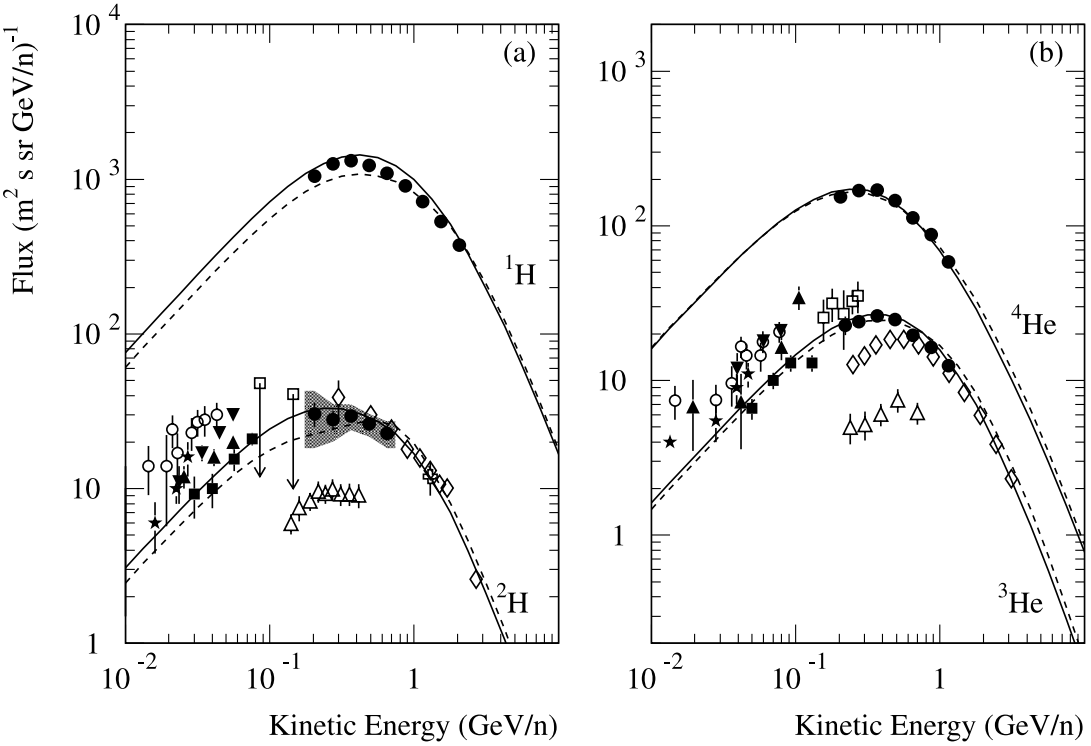

FIG. 13.—BESS 93 differential energy spectra (*filled circles*) at the top of atmosphere for (*a*) hydrogen isotopes, proton, and ^{2}H and (*b*) helium isotopes, ^{3}He, and ^{4}He, compared to other experimental data. The data points are as follows: *filled circles*: this work; *open diamonds*: de Nolfo et al. (2000), Menn et al. (2000); *open cross*: Bogomolov (1995); *open squares*: Leech & O'Gallagher (1978); *open upward-pointing triangles*: Webber et al. (1991); *filled downward-pointing triangles*: Beatty (1986); *open circles*: Webber & Yushak (1983); *filled stars*: Mewaldt, Stone, & Vogt (1976); *filled upward-pointing triangles*: Garcia-Munoz, Mason, & Simpson (1975a, 1975b); *filled squares*: Kroeger (1986). The solid curves represent calculated spectra using the reacceleration model with solar modulation parameter 700 MV. The dashed curves represent calculated spectra using the standard leaky-box model with solar modulation parameter 600 MV. The error bars show only the statistical uncertainty, while the shaded region indicates the total uncertainty of this measurement including systematic uncertainty.

TABLE 7

BESS 93 DEUTERON FLUXES AT THE TOP OF THE ATMOSPHERE

KINETIC ENERGY (GeV nucleon^{-1})		Deuteron Flux at TOA[a]
Interval	Mean	(m^2 s sr GeV nucleon^{-1})$^{-1}$
0.18–0.24	0.21	$(3.05 \pm 0.54 \pm 1.10) \times 10^1$
0.24–0.32	0.27	$(2.78 \pm 0.39 \pm 0.66) \times 10^1$
0.32–0.42	0.37	$(2.95 \pm 0.30 \pm 0.48) \times 10^1$
0.42–0.56	0.49	$(2.61 \pm 0.22 \pm 0.37) \times 10^1$
0.56–0.75	0.65	$(2.27 \pm 0.17 \pm 0.41) \times 10^1$

[a] Top of the atmosphere; the quoted errors include two parts: the statistical error and the systematic error.

TABLE 8

BESS 93 ^{3}He FLUXES AT THE TOP OF THE ATMOSPHERE

KINETIC ENERGY (GeV nucleon^{-1})		^{3}He Flux at TOA[a]
Interval	Mean	(m^2 s sr GeV nucleon^{-1})$^{-1}$
0.20–0.24	0.22	$(2.28 \pm 0.31 \pm 0.18) \times 10^1$
0.24–0.32	0.27	$(2.41 \pm 0.19 \pm 0.18) \times 10^1$
0.32–0.42	0.37	$(2.61 \pm 0.16 \pm 0.19) \times 10^1$
0.42–0.56	0.49	$(2.46 \pm 0.13 \pm 0.21) \times 10^1$
0.56–0.75	0.65	$(1.96 \pm 0.10 \pm 0.20) \times 10^1$
0.75–1.00.....	0.87	$(1.64 \pm 0.08 \pm 0.17) \times 10^1$
1.00–1.33.....	1.15	$(1.25 \pm 0.06 \pm 0.19) \times 10^1$

[a] Top of the atmosphere; the quoted errors include two parts: the statistical error and the systematic error.

were obtained from heavy secondary ratio (i.e., B/C) measurement. The agreement of the data with the calculated spectra indicates that the propagation history for light cosmic-ray nuclei, protons and helium nuclei, is not much different from that of the heavy nuclei.

As mentioned in § 3.2.4, we derived the hydrogen and helium energy spectra from the raw rigidity spectra by taking all hydrogen particles as protons and all helium particles as ^{4}He, as other authors have done in previous measurements. By utilizing the velocity information measured from the TOF in the BESS 93 flight, we can separate the hydrogen and helium individual isotopes with rigidities up to 3 GV. The separate proton, deuteron, ^{3}He, and ^{4}He energy spectra are presented in this section. By summing up the proton and deuteron fluxes and the ^{3}He and ^{4}He fluxes, respectively, and comparing them with hydrogen and helium fluxes shown in Tables 5 and 6, we can determine the error due to no isotope separation. This error is small ($\leq$2%) for hydrogen, while for helium spectra over the energy range below 1 GeV nucleon^{-1} the flux evolves from an overestimate at low energies by about 11% at 0.27 GeV nucleon^{-1} to an underestimate by about 3% at 1 GeV nucleon^{-1}. The results are consistent with the IMAX-92 ^{3}He and ^{4}He measurements (Menn et al. 2000).

4.3. *Ratios of* ^{2}H/^{1}H, ^{2}H/^{4}He *and* ^{3}He/^{4}He *at TOA*

The ^{2}H/^{1}H ratios of BESS 93 are shown in Figure 14*a*, and the ^{2}H/^{4}He, and ^{3}He/^{4}He ratios are compared with the

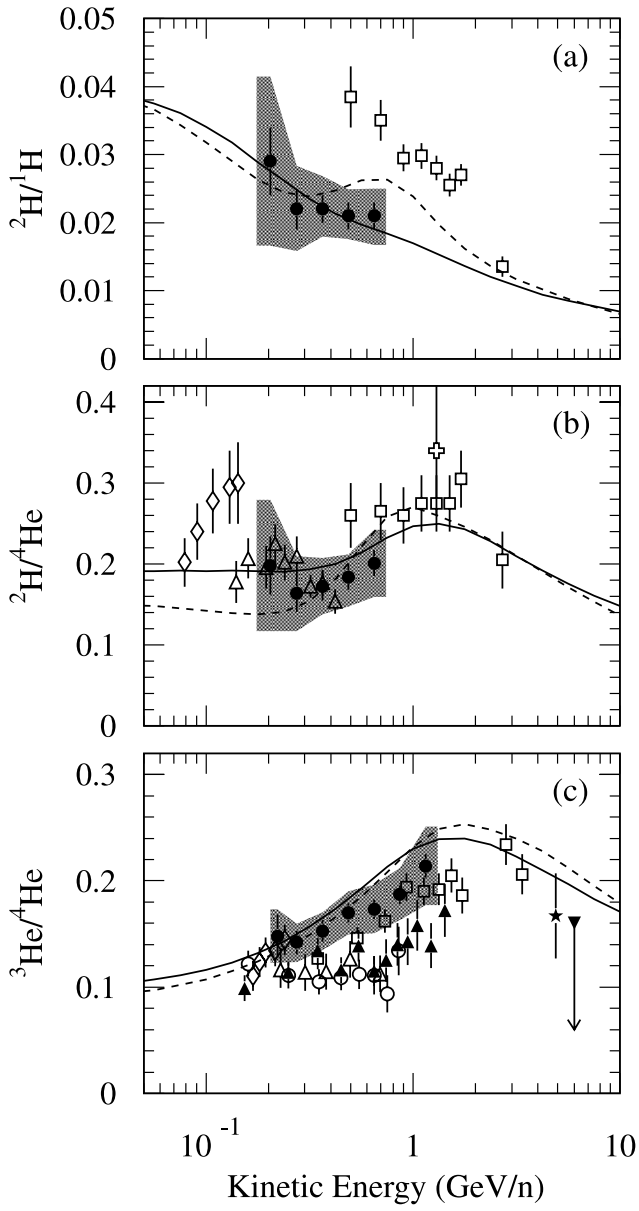

FIG. 14.—BESS 93 isotope flux ratio of (*a*) ^{2}H/^{1}H, (*b*) ^{2}H/^{4}He, and (*c*) ^{3}He/^{4}He at the top of atmosphere as a function of kinetic energy per nucleon, compared to other experimental data. The data points are as follows: *filled circles*: this work; *open squares*: IMAX measurements (Reimer et al. 1998; de Nolfo et al. 2000; $\phi = 750$ MV); *filled upward-pointing triangles*: SMILI-1 measurements (Beatty et al. 1993; $\phi = 1.2$ GV); *open circles*: SMILI-2 measurements (Wefel et al. 1995a; $\phi = 1.5$ GV); *open upward-pointing triangles*: MASS measurements (Webber et al. 1991; $\phi = 1.4$ GV); *open diamonds*: Webber & Yusak (1983; $\phi = 450$ MV); *star*: Hatano et al. (1995); *filled downward-pointing triangle*: Jordan & Meyer (1984), reanalyzed by Webber, Golden, & Mewaldt (1987; $\phi = 400$ MV); *open cross*: Bogomolov et al. (1995). The solid curves represent calculated spectra using the reacceleration model with solar modulation parameter 700 MV. The dashed curves represent calculated spectra using the standard leaky-box model with solar modulation parameters 600 MV. The error bars show only the statistical uncertainty, while the shaded regions indicate the total uncertainty of this measurement including systematic uncertainty.

previous measurements in Figures 14*b* and 14*c*, respectively. Again, the error bars show the statistical error only, and the shaded regions show the overall uncertainties of the measurements. The solid curves show the prediction of the reacceleration model with a solar modulation level of 700 MV. The dashed curves represent the SLBM calculated ratios with the modulation parameter 600 MV. The parameters for the ratio calculations are the same as these for the flux calculations shown in Figure 13. In general, within the overall uncertainty, the measurement results are consistent with the prediction of both models except for the ^{2}H/^{1}H ratio at high energy. Among these, the ^{2}H/^{1}H ratio is most sensitive to the propagation models, and our current results show a tendency of better agreement with the reacceleration model. The later BESS data extending to higher energies and having better precision will provide conclusive results.

5. CONCLUSION

The BESS 93 instrument had many outstanding hardware features that enabled precise measurements of cosmic-ray hydrogen and helium and their isotopes. To obtain the final precise energy spectra, this study emphasized in the following four aspects. First, the detection efficiency was corrected by using the latest available cross section data and their parameterizations, which show large energy dependencies at low energies. Because of insufficient experimental data, the cross section uncertainty of heavy-ion reactions dominates the overall uncertainty in many similar cosmic-ray measurements. In this study, we implemented the LaRC model for cross section parameterization, and it provides reasonably good agreement with the known experimental data. Second, the hadron simulation packages RQMD and FRITIOF were implemented in a GEANT-based simulation code. A complete simulation was performed not only for protons, but also for heavy ions, deuterons, and helium nuclei. Monte Carlo simulations were essential in the data analysis. They helped us to understand the instrument performance and to calculate the geometry factors; moreover, this was the only way to obtain the efficiency of the single-track cuts, since the incident fluxes were unknown. Third, the effect of δ-rays, which has a large influence on the measurement of high-energy heavy ions, was properly simulated in this study. Fourth, the secondary fluxes produced in the residual air above the instrument were calculated iteratively with the simultaneously measured primary cosmic-ray spectra. The corrections for singly charged particles are significant, up to 42% and 63%, respectively, for protons and deuterons at the lowest measured energies.

In this paper we have presented the BESS 93 measurements of the hydrogen and helium nuclei energy spectra from 0.2 to 10 GeV nucleon^{-1}, along with their isotopic composition between 0.2 and about 1 GeV nucleon^{-1}. The deuteron and ^{3}He fluxes were determined for the first time over this energy range in a time period of solar minimum. In general, the results of this experiment are consistent with but have better precision than other recent measurements of balloon-borne or satellite experiments. The overall uncertainties for measured hydrogen and helium fluxes at 1 GeV nucleon^{-1} are reduced to 4% and 7%, respectively. The measured spectra of protons, deuterons, ^{3}He, and ^{4}He and their corresponding ratios were compared with different interstellar/heliospheric propagation calculation and were found to be consistent with the reacceleration model for a solar modulation parameter close to $\phi = 700$ MV. This suggests that the light cosmic-ray elements, protons, deuterons, and helium nuclei, have a propagation history similar to that of the heavier nuclei. Ratios among these

isotopes indicate that our deuteron data prefer the reacceleration model at high energies. Better precision measurements with later BESS flights are expected to provide conclusive results.

The successive annual balloon flights of BESS since 1993 provide a unique opportunity to study hydrogen, helium, and their isotopic composition over nearly a complete solar cycle. Data from later BESS flights are being analyzed with a procedure similar to that presented in this study, and those results will be reported when they are available.

This work is supported in Japan by Grant-in-Aid for Scientific Research, Monbusho, and in the US by NASA grants NAGW-3526 and NAG 5-5061. We thank NSBF for balloon flight support. We also thank R. K. Tripathi at the NASA/LaRC for his support with the LaRC model.

REFERENCES

Abdullin, S. K., et al. 1992, Nucl. Phys. A, 569, 753
Ableev, V. G., et al. 1985, Acta Phys. Pol. B, 16, 913
Ajima, Y., et al. 2000, Nucl. Instrum. Methods Phys. Res. A, 443, 71
Aksinenko, V. D., et al. 1980, Nucl. Phys. A, 348, 518
Alcaraz, J., et al. 2000, Phys. Lett. B, 472, 215
Andersson, B., Gustafson, G., & Pi, H. 1993, Z. Phys. C, 57, 485
Auce, A., et al. 1994, Phys. Rev. C, 50, 871
Barkas, W. H., & Berger, M. J. 1964, Tables of Energy Losses and Ranges of Heavy Charged Particles (NASA SP-3013; Washington: NASA)
Barwick, S. W., et al. 1998, ApJ, 498, 779
Beatty, J. J. 1986, ApJ, 311, 425
Beatty, J. J., et al. 1993, ApJ, 413, 268
Bertsch, D. L., et al. 1993, ApJ, 416, 587
Boezio, M., et al. 1997, ApJ, 487, 415
———. 1999, ApJ, 518, 457
Bogomolov, E. A., et al. 1995, Proc. 24th Int. Cosmic-Ray Conf. (Roma, 1995), 2, 598
Brun, R., et al. 1984, GEANT User's Guide (CERN DD/EE/84-1; Geneva: CERN)
Carlson, R. F. 1996, At. Data Nucl. Data Tables, 63, 93
Circella, M., et al. 1997, Proc. 25th Int. Cosmic-Ray Conf. (Durban), 7, 117
Davis, A. J., et al. 1995, Proc. 24th Int. Cosmic-Ray Conf. (Rome), 2, 622
de Nolfo, G. A., et al. 2000, AIP Conf. Proc. 528, Acceleration and Transport of Energetic Particles Observed in the Heliosphere, ed. R. A. Mewaldt et al. (New York: AIP), 425
Dubar, C. V., et al. 1989, Soviet J. Nucl. Phys., 49, 771
Fisk, L. A., Forman, M. A., & Axford W. I. J. 1973, Geophys. Res., 78, 995
Garcia-Munoz, M., Mason, G. M., & Simpson, J. A. 1975a, Proc. 14th Int. Cosmic-Ray Conf. (Munich), 1, 319
———. 1975b, ApJ, 202, 265
Glagolev, V. V., et al. 1993, Z. Phys. C, 60, 421
Golden, R. L. 1996, ApJ, 457, L103
Hatano, Y., et al. 1995, Phys. Rev. D, 52, 6219
Hernandez, J. J., et al. 1990, Phys. Lett. B, 329, 1
Honda, M., et al. 1995, Phys. Rev. D, 52, 1985
Igo, G. J., et al. 1967, Nucl. Phys. B, 3, 181
Jaros, J., et al. 1978, Phys. Rev. C, 18, 2273
Jordan, S. P., & Meyer, P. 1984, Phys. Rev. Lett., 53, 505
Kim, H. J., et al. 1999, Proc. 26th Int. Cosmic-Ray Conf. (Salt Lake City), 1, 17
Kroeger, R. 1986, ApJ, 303, 816
Leech, H. W., & O'Gallagher, J. J. 1978, ApJ, 221, 1110
Maeno, T., et al. 2001, Astropart. Phys., 16, 121
Matsunaga, H., et al. 1998, Phys. Rev. Lett., 81, 4052
Menn, W., et al. 2000, ApJ, 533, 281
Mewaldt, R. A., Stone, E. C., & Vogt, R. E. 1976, ApJ, 206, 616
Meyer, J. P. 1972, A&AS, 7, 417
Mitchell, J. W., et al. 1996, Phys. Rev. Lett., 76, 3057
Moiseev, A., et al. 1997, ApJ, 474, 479
Montanet, L., et al. 1994, Phys. Rev. D, 50, 1173
Mori, M. 1997, ApJ, 478, 225
Nicholls, J. E., et al. 1972, Nucl. Phys. A, 181, 329
Nozaki, M., et al. 1999, Proc. 26th Int. Cosmic-Ray Conf. (Salt Lake City), 3, 85
Orito, S. 1987, ASTROMAG Workshop (KEK Report 87-19), 111
Orito, S., et al. 2000, Phys. Rev. Lett., 84, 1078
Ormes J. F., et al. 1997, ApJ, 482, L187
Papini, P., Grimani, C., & Stephens, S. A. 1993a, Proc. 23rd Int. Cosmic-Ray Conf. (Calgary), 1, 499
———. 1993b, Proc. 23rd Int. Cosmic-Ray Conf. (Calgary), 1, 503
———. 1993c, Proc. 23rd Int. Cosmic-Ray Conf. (Calgary), 3, 761
———. 1996, Nuovo Cimento, 19, 367
Reimer, O., et al. 1998, ApJ, 496, 490
Rygg, T. A., & Earl, J. A. 1971, J. Geophys. Res., 76, 7445
Saeki, T., et al. 1998, Phys. Lett. B, 422, 319
Sanuki, T., et al. 2000, ApJ, 545, 1135
Seo, E. S., & Ptuskin, V. S. 1994, ApJ, 431, 705
Seo, E. S., et al. 1991, ApJ, 378, 763
———. 1994, ApJ, 432, 656
———. 1995, Proc. 24th Int. Cosmic-Ray Conf. (Rome), 2, 648
———. 1997a, Adv. Space Res., 19, 751
———. 1997b, Proc. 25th Int. Cosmic-Ray Conf. (Durban), 3, 373
———. 2000, Adv. Space Res., 26, 1831
Sorge, H. 1995, Phys. Rev. C, 52, 3291
Tanihata, I., et al. 1985, Phys. Lett. B, 160, 380
Tripathi, R. K., Cucinotta, F. A., & Wilson, J. W. 1996, Nucl. Instrum. Methods B, 117, 347
Velichko, G. N., et al. 1985, Soviet J. Nucl. Phys., 42, 837
Wang, J. Z., et al. 1999, Proc. 26th Int. Cosmic-Ray Conf. (Salt Lake City), 3, 37
Webber, W. R. 1997, Adv. Space Res., 19, 755
Webber, W. R., Golden, R. L., & Mewaldt, R. A. 1987, ApJ, 312, 178
Webber, W. R., & Yushak, S. M. 1983, ApJ, 275, 391
Webber, W. R., et al. 1990, Phys. Rev. C, 41, 520
———. 1991, ApJ, 380, 230
Wefel, J. P., et al. 1995a, 24th Int. Cosmic-Ray Conf. (Rome), 2, 630
———. 1995b, 24th Int. Cosmic-Ray Conf. (Rome), 2, 634
Yamamoto, A., et al. 1994, Adv. Space Res., 14, 75
Yoshimura, K., et al. 1995, Phys. Rev. Lett., 75, 3792